

Ferhun C. Caner

Visiting Scholar at Northwestern University
Associate Professor
Institute of Energy Technologies,
Technical University of Catalonia,
Diagonal 647,
E-08028 Barcelona, Spain
e-mail: ferhun.caner@upc.edu

Zdeněk P. Bažant

Professor McCormick Institute
W.P. Murphy Professor of Civil Engineering
and Materials Science
Northwestern University,
2145 Sheridan Road,
CEE/A135,
Evanston, IL 60208
e-mail: z-bazant@northwestern.edu

Christian G. Hoover

Graduate Research Assistant
Department of Civil and Environmental
Engineering,
Northwestern University,
2145 Sheridan Road,
Evanston, IL 60208
e-mail: christianhoover2010@
u.northwestern.edu

Anthony M. Waas

Felix Pawlowski Collegiate Professor
Department of Aeronautical Engineering,
University of Michigan,
3044 FXB Building,
1320 Beal Avenue,
Ann Arbor, MI 48109
e-mail: dcw@umich.edu

Khaled W. Shahwan

Chairman of ACC100 Group and Member
of the Board of Directors of Automotive
Composites Consortium (ACC/USCAR)
Chrysler Technology Center,
Chrysler Group LLC,
Auburn Hills, MI 48326-2757
e-mail: kws8@chrysler.com

Microplane Model for Fracturing Damage of Triaxially Braided Fiber-Polymer Composites

A material model for the fracturing behavior for braided composites is developed and implemented in a material subroutine for use in the commercial explicit finite element code ABAQUS. The subroutine is based on the microplane model in which the constitutive behavior is defined not in terms of stress and strain tensors and their invariants but in terms of stress and strain vectors in the material mesostructure called the "microplanes." This is a semi-multiscale model, which captures the interactions between inelastic phenomena such as cracking, splitting, and frictional slipping occurring on planes of various orientations though not the interactions at a distance. To avoid spurious mesh sensitivity due to softening, the crack band model is adopted. Its band width, related to the material characteristic length, serves as the localization limiter. It is shown that the model can realistically predict the orthotropic elastic constants and the strength limits. More importantly, the present model can also fit the tests of size effect on the strength of notched specimens and the post-peak behavior, which have been conducted for this purpose. When used in the ABAQUS software, the model gives a realistic picture of the axial crushing of a braided tube by a divergent plug. [DOI: 10.1115/1.4003102]

1 Introduction

Lightweight composites with braided fiber reinforcements have the advantage of a relatively high specific energy absorption. This feature is especially pronounced for two-dimensional triaxially braided composites (2DTBCs), which have recently been considered for primary structural applications in automotive designs. The 2DTBCs are usually made up of several layers of polymer matrix, each of them reinforced by axial tows and bias tows of two opposite in-plane inclinations. The objective of this study is to model the stiffness, strength, and fracturing behavior of the 2DTBC, including the size effects.

In the compression crushing process of a braided composite, cracking of the matrix is accompanied by buckling and kinking of the embedded tows followed by breakage of the tows [1–5]. These

damage modes are strongly influenced by the geometry of the braid. Emphasis is placed both on the in-plane orientation of the tows and the height-to-length ratio of the wave of their undulation in the out-of-plane direction. The undulation of the axial and braider tows has a strong effect on the axial stiffness of the composite and the local buckling strength of the embedded tows, as suggested by the analysis in Refs. [6,7] and experimentally confirmed in Refs. [1,2,8].

The strong mechanical link between the braid geometry and the macroscopic stiffness, strength and energy absorption makes micromechanical modeling suitable for describing the fracture process of these composites. A detailed mesoscale analysis based on the finite element analysis can provide useful insight in the fracture process of braided composites [2,9,10]. However, this type of mesoscale analysis can be computationally expensive, often fails to converge, and does not allow the dominant features of macroscopic behavior to be easily extracted [11,12].

Alternative previous approaches describe the response of

Manuscript received November 16, 2009; final manuscript received September 16, 2010; published online March 24, 2011. Assoc. Editor: Hussein Zbib.

braided composites phenomenologically by means of macroscopic constitutive models used within the framework of classical continuum damage mechanics. For these models, the material model parameters were not directly related to the geometry of the composite mesostructure and must be determined by a strictly empirical fitting of the results for each particular type of composite with different braid angles, undulation wave heights, fiber contents, etc.

This study presents the development of a microplane constitutive model for the elastic behavior and distributed fracturing of the 2DTBC. The microplane approach is computationally less expensive, conceptually clearer, and more robust than a fully multiscale approach while being able to resolve the details of damage better than the classical tensorial constitutive models.

2 Microplane Model for Braided Composites

The microplane model has already been very successful for other quasi-brittle materials (concrete, rock, soils, foams, and composites laminated from unidirectional prepregs) [13–25]. In this model, the constitutive behavior is described not by tensors and their invariants but by stress and strain vectors on planes (or “microplanes”) of various representative orientations in the material microstructure. The advantage is that the model can approximately capture the basic physical phenomena having distinct orientations in the mesostructure. This is particularly important for the cracking damage in the 2DTBC in tension and compression. Another advantage is that the energy dissipation is captured separately for planes of various orientations in the microstructure. This facilitates modeling, and is useful for maximizing the energy dissipation as a sum of energy dissipations on all the microplanes.

The inelastic phenomena in the representative unit cell (RUC) of material in the microplane model are collapsed into one macrocontinuum point, but their orientations are preserved. Thus, the microplane model is semi-multiscale—it captures interactions among various orientations though not the interactions at a distance that are exhibited by nonlocal damage models [26].

The fracturing of the matrix is rather diffuse and multidirectional, and so the matrix does not necessitate the microplane model. It may simply be described by the isotropic damage model, as recently used in Ref. [27]. The tows, on the other hand, act in defined directions and thus are described by the microplane approach. The input parameters are related to the geometry and mechanical properties of the components of the composites. However, the link to the mesoscale makes possible an easier and clearer determination of these parameters.

2.1 Elastic Behavior. Although they are made of transversely isotropic fiber tows embedded in isotropic matrix, the triaxially woven composites are known to exhibit orthotropic elasticity due to the specific orientation and situation of various components that cannot be overlooked [28–33].

The macroscopic constitutive model consists of four components representing the mechanical response of matrix, the axial tows, and the left and right braider tows. The axial tows and the matrix that connect them are assumed to form a plate. In such a plate, in the axial direction, the axial tows and the matrix in between the axial tows are coupled in parallel. But in the lateral direction, they are coupled in series. The inclined tows are assumed to be coupled in parallel to this axial tow/matrix tow plate.

The geometries of the axial tows and the left and right braider tows are particularly suitable for microplane modeling because the distinct directional aspects of the undulation and tow braiding can be captured separately. With respect to stiffness, the main effect of the tow undulation is that the axial force in the tow direction produces shear forces on planes of varying inclinations normal to the tow of varying slope. By identifying the inclined planes with the microplanes, the shear forces are automatically reproduced on the microplanes. Ideally, the planes of all inclinations could be represented by the microplanes but for the sake of simplicity, it suffices to sample among all the possible inclinations only three.

This is done by three microplanes whose normals correspond to the mean, minimum, and maximum slopes of the tows within each wavelength. These inclinations automatically induce out-of-plane stresses produced by the axial forces acting along an undulating tow.

To determine the stress tensor that corresponds to a given strain tensor, first, the normal strain on a microplane may be calculated,

$$\varepsilon_N = N \cdot \varepsilon \cdot N \quad (1)$$

where N is the normal vector of the microplane.

The normal stress σ_N that corresponds to this normal strain is given by the constitutive relation

$$\sigma_N = E_N \varepsilon_N \quad (2)$$

where E_N is the elastic normal stiffness corresponding to the microplane. The stress tensor for any fiber tow would then be given by

$$\sigma = \frac{1}{3} \sum_{\nu=1}^3 \sigma_N N_\nu \otimes N_\nu \quad (3)$$

where subscript $\nu=1, 2, 3$ labels the typical directions of undulation for a given fiber tow. In addition, any inclination of such tows with respect to the global system of axes should be taken into account separately. We note that, in fact, a higher level microplane model could also be constructed in which the fiber tows of various inclinations are represented on microplanes whose orientations coincide with the orientations of these tows. Then, the above equation could be applied recursively. However, in what follows, we construct microplane models for individual structural elements that constitute the braided composite. For simplicity, we choose not to pursue a higher order microplane model and instead directly assemble the contributions from these structural components in accordance with general mechanics principles.

According to the microplane concept, the stiffness matrix for the undulating axial fiber tows represented by three microplanes (labeled by $\mu=1, 2, 3$) is given by (superscript or subscript “f” generally refers to fiber tows)

$$K^{\text{axt}} = V_f \frac{1}{3} \sum_{\mu=1}^3 [E_{\text{axial}}^f N_\mu^{\text{axt}} \otimes N_\mu^{\text{axt}} \otimes N_\mu^{\text{axt}} \otimes N_\mu^{\text{axt}} + E_{\text{lateral}}^f (M_\mu^{\text{axt}} \otimes M_\mu^{\text{axt}} \otimes M_\mu^{\text{axt}} \otimes M_\mu^{\text{axt}} + L_\mu^{\text{axt}} \otimes L_\mu^{\text{axt}} \otimes L_\mu^{\text{axt}} \otimes L_\mu^{\text{axt}})] + (1 - V_f) K_m \quad (4)$$

in which V_f is given with respect to one axial fiber tow, $N_\mu^{\text{axt}}, M_\mu^{\text{axt}}, L_\mu^{\text{axt}}$ form a system of rectangular coordinates at a generic microplane μ , E_{axial}^f and E_{lateral}^f are the axial and lateral elastic moduli of the fibers only, respectively, and finally, K_m is the stiffness tensor of the isotropic polymer matrix inside one undulating axial tow. By inverting K^{axt} , one can obtain the compliance from which the elastic properties $E_1^{\text{axt}}, E_2^{\text{axt}}, E_3^{\text{axt}}, \nu_{12}^{\text{axt}}/E_1^{\text{axt}}, \nu_{13}^{\text{axt}}/E_1^{\text{axt}}$, and $\nu_{23}^{\text{axt}}/E_2^{\text{axt}}$ of the undulating axial tows can be inferred.

Various mesomechanical simulations [34] suggested that the matrix between the axial tows works in transferring loads in the lateral direction and stiffens the axial response. Approximately, the matrix between the axial tows works in parallel coupling with the axial tows in axial loading direction, but in series coupling with the axial tows in the lateral loading direction. This fact cannot be overlooked because otherwise it would be impossible to correctly model the axial stiffnesses in the two directions using the same set of elementary properties for the constituents. The fiber tows are permeated by the polymer matrix bonding the fibers, and that part of the matrix must be treated as part of the tow. Since recent research indicates that the properties of the polymer matrix phase on the microscale within the tows are not the same [35] as those of the matrix phase in the bulk between the tows (which can only be explained by dominance of interface effects of the fibers), a different stiffness should be used for the tow matrix.

Table 1 Elastic properties of various constituents of the 2DTBC used in the model

| Braider angles | $\phi=30, 45, 60$ (deg) |
|---|-------------------------|
| E_m for the matrix, MPa | 7520 |
| ν_m for the matrix | 0.36 |
| E_{ax} for axial tows, MPa | 115,900 |
| E_{it} for inclined tows, MPa | 102,050 |
| V_{axt} for axial tows | 0.408 |
| V_{axm} for the matrix between axial tows | 0.272 |
| V_{it} for inclined tows | 0.120 |
| V_m for the matrix between layers | 0.200 |

However, the same properties are assumed here since the effect of the difference is numerically equivalent to adjusting the volume subdivision between the tow matrix and the bulk matrix, which is calibrated empirically.

The tow matrix is considered to have the same undulation as the tow itself. In any given undulation direction, the plate consisting of the axial tow and the matrix tow must have elastic behavior that reflects the parallel coupling in the axial direction and series coupling in the lateral direction. Such couplings lead to the following elastic orthotropic constitutive equations for the axial tow plate:

$$\begin{Bmatrix} \varepsilon_1 \\ \varepsilon_2 \\ \varepsilon_3 \end{Bmatrix} = \begin{bmatrix} 1/E_1 & -\nu_{21}/E_2 & -\nu_{31}/E_3 \\ -\nu_{12}/E_1 & 1/E_2 & -\nu_{32}/E_3 \\ -\nu_{13}/E_1 & -\nu_{23}/E_2 & 1/E_3 \end{bmatrix}^{axtp} \begin{Bmatrix} \sigma_1 \\ \sigma_2 \\ \sigma_3 \end{Bmatrix} \quad (5)$$

along with $\gamma_i = \sigma_i / G_i^{axtp}$ for $i=4, 5, 6$ where

$$E_1^{axtp} = V_{axt} E_1^{axt} + V_{axm} E_m$$

$$E_2^{axtp} = \left(\frac{V_{axt}}{E_2^{axt}} + \frac{V_{axm}}{E_m} \right)^{-1}$$

$$E_3^{axtp} = V_{axt} E_3^{axt} + V_{axm} E_m$$

$$\nu_{12}^{axtp} = E_1^{axtp} \left(\nu_{12}^{axt} \frac{V_{axt}}{E_1^{axt}} + \nu_m \frac{V_{axm}}{E_m} \right)$$

$$\nu_{13}^{axtp} = E_1^{axtp} \left(\nu_{13}^{axt} \frac{V_{axt}}{E_1^{axt}} + \nu_m \frac{V_{axm}}{E_m} \right)$$

$$\nu_{23}^{axtp} = E_2^{axtp} \left(\nu_{23}^{axt} \frac{V_{axt}}{E_1^{axt}} + \nu_m \frac{V_{axm}}{E_m} \right)$$

$$G_4^{axtp} = \left(\frac{V_{axt}}{G_4^{axt}} + \frac{V_{axm}}{G_m} \right)^{-1}$$

$$G_5^{axtp} = \left(\frac{V_{axt}}{G_5^{axt}} + \frac{V_{axm}}{G_m} \right)^{-1}$$

$$G_6^{axtp} = V_{axt} G_6^{axt} + V_{axm} G_m$$

where $E_1, E_2, E_3, G_4, G_5, G_6$ =macroscopic axial and shear elastic moduli of the braided composite for the three directions of orthotropy, ν_{ij} =orthotropic Poisson's ratios, and V denotes the volume fractions in the composite. The superscripts or subscripts have the following meanings: "m" is matrix, "axt" is axial tows, "it" is inclined tows, "ax" is axial, "axm" is matrix between axial tows, "axtp" is axial tow plate. E_m, ν_m =Young's modulus and Poisson's ratio for the polymer matrix, respectively, and E_{ax}, E_{it} =axial elastic moduli of the axial and inclined tows, respectively. The values of material constants for the constituents of the 2DTBC used as input in the calculations are shown in Table 1.

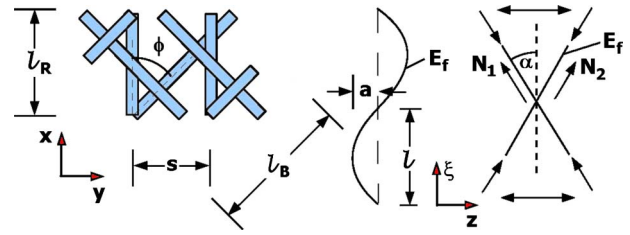


Fig. 1 The geometry of RUC for the 2DTBC and its idealization in microplane model

Similarly, using only three microplanes that describe the undulation of the inclined braids, the stiffness of the left and right inclined braids can be obtained as

$$K^{lit} = \frac{1}{3} \sum_{\mu=1}^3 E_{it} N_{\mu}^{lt} \otimes N_{\mu}^{lt} \otimes N_{\mu}^{lt} \otimes N_{\mu}^{lt}$$

$$K^{rit} = \frac{1}{3} \sum_{\mu=1}^3 E_{it} N_{\mu}^{rt} \otimes N_{\mu}^{rt} \otimes N_{\mu}^{rt} \otimes N_{\mu}^{rt} \quad (6)$$

Based on the volume fraction of each constituent, the total axial stress in the braided composite may then be written as

$$\sigma = [1 - V_{axtp} - 2V_{it}] \sigma_m + V_{axtp} \sigma_{axtp} + V_{it} (\sigma_{lit} + \sigma_{rit}) \quad (7)$$

where the volume fractions are with respect to the braided composite as a whole. The first term in this equation refers to the thin matrix layers located between the axial tow and the inclined braider tows and constitutes a relatively small fraction of the total volume.

The in-plane and out-of-plane geometries of the braids are shown on the left and right of Fig. 1, respectively (where $l_R = 10$ mm and $l_B = 20$ mm for 30 deg braided composite, $l_R = 13.28$ mm and $l_B = 18.78$ mm for 45 deg braided composite, and $l_R = 18.2$ mm and $l_B = 21.01$ mm for 60 deg braided composite). Let ϕ be the angle between the braider and axial tows, and s be the spacing of the axial tows. Then, the length of the center-lines of the axial and braider tows contained within a RUC can be calculated as $l_R = s / \tan \phi$ and $l_B = s / \sin \phi$, where l_R and l_B = lengths projected onto the middle plane of composite. As a simplification, the undulation can be assumed to follow a sine curve with the average imperfection amplitudes of a and a_b for the axial and braider tows, respectively. Further, let l be the half-wavelength of the tow over one RUC, and let a be the amplitude that is measured on the appropriate specimen sections [3]. The braider tow is assumed to be completely contained inside the laminate. When no laboratory measurements are available, the braider amplitude can conservatively be taken as $l/2$, where l is the total (final) thickness of one layer of the cured composite braider laminate.

Based on the parameter values given in Table 1, the model yields the elastic constants for the 2DTBCs with three different inclination angles of the inclined braids; see Table 2.

2.2 Cohesive Fracturing Behavior. In the cohesive fracturing model chosen for the microplane analysis of 2DTBC fracture, all the components of the stress tensor in the matrix are assumed to be reduced in the same ratio by a scalar damage parameter. Compared with the previous microplane models, this is a simplifying assumption that has been justified by matching various test results. Since fiber damage dominates the overall damage [1], the polymer matrix plays a secondary role, which is why an isotropic damage model for the polymer matrix is sufficient. The cracking orientation is essential for the tows but not the matrix. Besides, this simplification has also the advantage of easier programming and computational robustness. Despite this simplifying assump-

Table 2 Elastic constants predicted by the microplane model and experimental results for comparison

| Elastic constants | $\phi=30$ deg | $\phi=45$ deg | $\phi=60$ deg | $\phi=45$ deg [2] experimental |
|-------------------|---------------|---------------|---------------|--------------------------------|
| ν_{21} | 0.143 | 0.144 | 0.149 | 0.36 |
| ν_{31} | 0.140 | 0.122 | 0.129 | – |
| ν_{23} | 0.110 | 0.114 | 0.120 | – |
| E_1 (MPa) | 67,604 | 64,172 | 64,188 | $68,530 \pm 12,000$ |
| E_2 (MPa) | 9709 | 11,306 | 15,972 | $10,780 \pm 2400$ |
| E_3 (MPa) | 10,300 | 10,355 | 10,334 | – |
| G_{12} (MPa) | 2500 | 2797 | 2583 | 7520 ± 2200 |
| G_{13} (MPa) | 1828 | 1814 | 1808 | – |
| G_{23} (MPa) | 1042 | 1048 | 1024 | – |

tion, the model is quite flexible. Varying the choice of the evolution law for the damage variable can produce a wide range of failure modes. This law has the form

$$\sigma^e = K^e : \varepsilon$$

$$\sigma = (1 - \omega)\sigma^e \quad (8)$$

where ω is the damage variable ($0 < \omega \leq 1$), K^e is the elastic stiffness tensor for the 2DTBC, and σ^e is the elastic stress tensor. This kind of damage has been used with success in a study of the size effect on delamination fracture driven by imperfection buckling of stiff composite skins bonded to a soft foam core of sandwich plate [27] (in that problem, too, the fracture orientation in the foam is restricted, being dominated by the skin-foam interface).

The size effect on structural strength is defined as the dependence of the nominal strength $\sigma_N = P_{\max}/A$ on the size D of “geometrically similar,” similarly loaded, structures, where P_{\max} = maximum load (peak) and A = area of a homologous characteristic cross section of the structure. It has been proven [36,37] that when the material failure criterion is given solely in terms of a critical stress (material strength) or critical strain or both, σ_N is always independent of D ; i.e., there is no size effect.

When, however, the material failure criterion also contains the energy per unit area (the fracture energy G_F) or, equivalently, a characteristic length l_{ch} (or the effective size of the fully developed fracture process zone, which may here be taken as the size of the RUC), then σ_N decreases with D . This decrease may in general be approximately described by Bažant’s size effect law [36–39] provided that a large crack or crack band develops before the maximum load or that the specimen has a large notch. This law represents a smooth transition from the case of no size effect for $D \rightarrow 0$ (as in the strength theory) to the maximum possible size effect for $D \rightarrow \infty$. The latter is the case of linear elastic fracture mechanics (LEFM) in which case the cross section of structure is far larger than l_{ch} .

The computational models that do not take G_F or l_{ch} into account generally miss the size effect and can thus be rather misleading. Measuring the size effect in geometrically similar notched specimens of quasi-brittle material is the simplest and most unambiguous way to determine G_F and l_{ch} .

When the failure occurs right at the initiation of macrofracture from a smooth surface, a deterministic size effect of a different type occurs provided that l_{ch} is not negligible compared with the structure. If it is negligible, the Weibull statistical size effect, due to material strength randomness, becomes dominant [36,37,39]. However, this type of size effect, which characterizes maximum loads reached at macro-crack initiation, is not relevant for the present problem and applications.

Although, for the simulation of size effect tests, the isotropic damage formulation has been found to suffice, there is no reason for the damage in axial, lateral, and transverse directions to be the same. Given the orthotropy of material strength and stiffness and

the difference in principal strains, it is better and not too difficult to allow the damage to be different for each direction. Therefore, for a general purpose model, we introduce damage variables $\omega_1, \omega_2, \omega_3$ with independent evolution in the principal planes of orthotropy, $i = 1, 2, 3$,

$$\sigma_{ii} = (1 - \omega_i)\sigma_{ii}^e \quad (9)$$

where the repeated indices do not imply summation.

For the shear components on these planes, the damage evolution was initially considered as in the form $\sigma_{ij} = [1 - \max(\omega_i, \omega_j)]\sigma_{ij}^e$, where $i, j = 1, 2, 3$. It was found, though, that this formulation of damage due to shear stresses would not predict the failure modes accurately, and so a different form of damage has been adopted,

$$\sigma_{ij} = (1 - \omega_i^m)(1 - \omega_j^m)\sigma_{ij}^e \quad (10)$$

where $i, j = 1, 2, 3$ and m is an empirical exponent. Computationally, the value of $m = 12$ is found to lead to agreement with the observation that the size effect test specimens described in a parallel study [34] develop shear damage modes only in the post-peak regime. For larger values of m , a mixed shear-tension failure, which was not the observed failure mode, is obtained in simulations. When m is near unity, all specimens in the size effect test simulations fail by tension, as observed in the tests, but the failure planes still transmit large shear stresses, which is not realistic. When $m = 12$ is used, the damage is tensile up to the peak load but in the post-peak, some mixed shear-tension type failure may be obtained in simulations.

Equation (10) thus realistically simulates the observed fracturing process in which tensile fracture on a plane must affect the shear resistance on the same plane. For the opening mode of failure, however, this shear-tension coupling formulation affects only the post-peak behavior when m is sufficiently large. Although this seems to be unnecessary for the simulation of size effect tests, for a general three-dimensional analysis, a realistic shear-tension coupling would be important for predicting the correct fracture paths, peak loads, and deformations.

The damage variables ω_i are functions of history variable γ , which is defined as the maximum effective strain ε_{eff} that has been reached during the previous history. It is expressed as $\gamma(t) = \max \varepsilon_{\text{eff}}(\tau)$ for $\tau \leq t$ (where t or τ denotes the time). The effective strain is defined as

$$\varepsilon_{\text{eff}} = \sqrt{\langle \varepsilon^I \rangle^2 + \langle \varepsilon^{\text{II}} \rangle^2 + \langle \varepsilon^{\text{III}} \rangle^2} \quad (11)$$

where $\langle x \rangle = \max(x, 0)$ and $\langle \varepsilon^I \rangle, \langle \varepsilon^{\text{II}} \rangle, \langle \varepsilon^{\text{III}} \rangle$ are the positive parts of the three principal strains. This definition of damage corresponds to a Rankine-type strength envelope with a smooth round-off in the sectors of two positive in-plane principal stresses. This evolution law can be used for compressive, tensile, or shear damage of the material. However, it was found that this simple damage definition causes the simulated notched 2DTBC specimens under

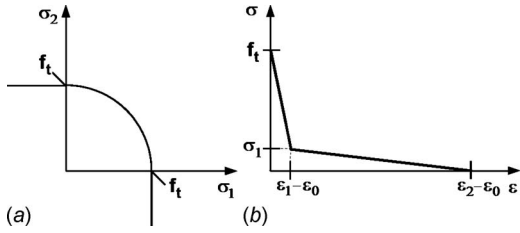


Fig. 2 Constitutive law for the matrix: (a) strength envelope in the biaxial stress plane and (b) bilinear softening law

three-point bending to fracture in shear, which is unrealistic. To prevent such computer simulation results, the argument of the history variable is modified as follows:

$$\varepsilon_{\text{eff}} = c \sqrt{\langle \varepsilon^{\text{I}} \rangle^2 + \langle \varepsilon^{\text{II}} \rangle^2 + \langle \varepsilon^{\text{III}} \rangle^2} + \frac{1-c}{3} (\langle \varepsilon^{\text{I}} \rangle + \langle \varepsilon^{\text{II}} \rangle + \langle \varepsilon^{\text{III}} \rangle) \quad (12)$$

For $c=0$, the evolution law leads to tensile failure only, while for $c=1$, the shear failure can also be simulated. In the 2DTBC simulations, reasonable results are obtained using $c \leq 0.05$ and $c = 0.01$ appears to be the optimal value.

The history dependence of damage variable ω is defined as follows:

$$\omega = g(\gamma) = \begin{cases} 0 & \text{if } \gamma \leq \varepsilon_0 \\ \frac{\varepsilon_1 - \sigma_1/E_m}{\varepsilon_1 - \varepsilon_0} \left(1 - \frac{\varepsilon_0}{\gamma} \right) & \text{if } \varepsilon_0 \leq \gamma \leq \varepsilon_1 + \varepsilon_0 \\ 1 - \frac{\sigma_1/E_m}{\varepsilon_2 - \varepsilon_1} \left(\frac{\varepsilon_2}{\gamma} - 1 \right) & \text{if } \varepsilon_1 + \varepsilon_0 \leq \gamma \leq \varepsilon_2 + \varepsilon_0 \\ 1 & \text{if } \gamma > \varepsilon_2 + \varepsilon_0 \end{cases} \quad (13)$$

Here, $\varepsilon_0 = f_t/E_m$, where f_t =tensile strength and E_m =modulus of elasticity of the matrix. The parameters $\varepsilon_1, \varepsilon_2, \sigma_1$ and f_t are related to the fracturing energy per unit width and area (i.e., per unit volume) of the crack band, which is

$$g_F = \frac{1}{2}(f_t + \sigma_1)(\varepsilon_1 - \varepsilon_0) + \frac{1}{2}\sigma_1(\varepsilon_2 - \varepsilon_1) \quad (14)$$

This equation corresponds to a damage law in the form of a bilinear curve of the transverse stress versus the average strain across the band (i.e., the crack opening divided by the crack band width), see Fig. 2.

3 Validation and Calibration by Test Data on Elastic Stiffness, Strength, and Size Effect

A program of the present formulation has been introduced into ABAQUS/EXPLICIT [40] as a VUMAT subroutine. First, it was verified that the computational model is robust, i.e., never fails during the computer simulation (unless the input is totally unreasonable). The robustness has been a general feature of microplane models for many other materials running under explicit integration of the equations of motion [13,41,42].

To validate and calibrate the model, three-point bend tests of size effect [43–48] were conducted [49] using geometrically similar notched specimens of the same type as standardized for concrete by RILEM (Réunion internationale des laboratoires d'études et d'essai des matériaux) [37,50]. The braider angles in the tests were $\phi=30$ deg, 45 deg, and 60 deg. The parameters that gave the best fits of the aforementioned size effect tests are shown in Table 3.

To avoid excessively localized damage and spurious mesh sensitivity, which are problems accompanying the size effect, the microplane model for 2DTBC is applied in the sense of the crack band model [19,37]. In that model, the strain average over the

Table 3 Fracturing parameters employed in the microplane model for the 2DTBC

| Fracture parameters | $\phi=30$ deg | $\phi=45$ deg | $\phi=60$ deg |
|---|------------------------|------------------------|------------------------|
| f_t for the matrix, MPa | 12.0 | 12.0 | 16.0 |
| σ_1 , MPa | 11.5 | 11.5 | 15.5 |
| ε_1 | 6×10^{-3} | 3.0×10^{-3} | 1.6×10^{-3} |
| ε_2 | 10×10^{-3} | 6.0×10^{-3} | 5×10^{-3} |
| ε_0 at initiation of fracture | 1.596×10^{-3} | 1.596×10^{-3} | 2.128×10^{-3} |
| Fracture energy, G_F , MPa mm | 0.747 | 0.337 | 0.264 |

crack band width is used and it is assumed that there exists one optimum finite element size that corresponds to the actual crack band width h . From observations, this width is roughly equal to l_{ch} , which roughly coincides with the RUC width and serves as the localization limiter. If larger or smaller finite elements need to be used, the post-peak part of the response of the microplane model is adjusted [51] so as to ensure the same energy dissipation per unit length of the propagating crack band. This is not necessary in the present problem so the element size in the transverse direction (i.e., perpendicular to the axial tows and the dominant crack propagation direction in the specimens) is taken to be equal to the RUC width, which roughly represents the width h of the propagating crack band.

The crack band model is a simpler substitute for using a non-local damage continuum [37]. The main objective of the nonlocal models is to allow element sizes much smaller or larger than the actual crack band width h without causing spurious mesh sensitivity and incorrect fracture energy dissipation. But such a refinement is not needed for the present problem. Achieving approximate mesh independence with the crack band model is simpler, in fact, much simpler, if the element size is kept equal to h . Changes in the finite element size appear to be unnecessary for the present problem.

The proper width of crack band and of the element size can be determined from size effect tests. It has thus been determined as 10 mm in the direction perpendicular to the crack propagation direction. This size must be considered together with the cohesive softening law defined by the parameters given in Table 3 in the sense of crack band model. Thus, the element size within the fracturing damage zone can be increased or decreased only if the cohesive softening law is scaled horizontally to yield the same fracture energy in all cases (an effective detailed procedure, used in a recently developed commercial code, is presented in Ref. [51]). In the present simulations, all the elements that lie along the crack path have exactly this size. The material fracture energies obtained from the best fits of the size effect test data are shown in Table 3.

To obtain the values f_t , σ_1 , ε_1 , and ε_2 shown in Table 3 for arbitrary types of fibers, matrices, and braiding angles, one must first specify the constituent properties. Next, one must perform size effect tests of three geometrically similar notched specimens. It must be ensured that the smallest specimen is small enough and the largest is large enough compared with the size of one RUC (this condition is verified if the test results fall into the transitional size of size effect curve, which is what has happened). Since the characteristic material length of the braided composites is relatively small, a large enough specimen can always be produced and tested.

By virtue of using the size effect law, only the peak loads for different sizes are needed for identifying the material fracture properties [37,50]. This makes the tests rather straightforward. The tensile strength of the matrix, f_t , may differ from that reported by the manufacturer, and thus it needs to be determined when fitting the peak loads obtained from the size effect tests (the most effective procedure for that is given in Ref. [52]). The strain at fracture initiation depends on f_t and can be approximated as ε_0

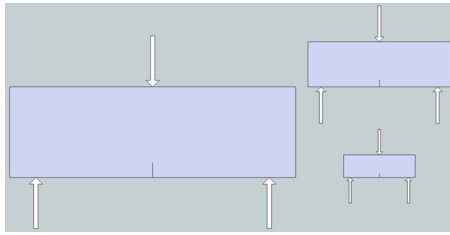


Fig. 3 The geometry of the specimens and loading configuration of the size effect tests conducted (for small, medium, and large sizes, the dimensions were $D=76.2$ mm, 152.4 mm, and 304.8 mm; $L=241.3$ mm, 482.6 mm, and 965.2 mm; $L'=196.85$ mm, 393.7 mm, and 787.4 mm; $a=12.7$ mm, 25.4 mm, and 50.8 mm; the out-of-plane thickness $t=7.62$ mm for all sizes)

$=f_t/E_m$, where E_m is the elastic modulus of the matrix. Once σ_1 , ε_1 , ε_2 , and f_t are determined, the cohesive fracturing curve is defined, and only the area under this curve needs to be calculated to determine the fracture energy, G_F .

Figure 3 shows the test results for the notched three-point bend specimens of three different sizes. Figures 4–6 show the experimental data for the notched three-point bend specimens of sizes (or depths) $D=76.2$ mm, 152.4 mm, and 304.8 mm (the span-to-depth ratio is 2.58). Also shown are the simulation results, corresponding to 2DTBCs with the inclined braider tows at angle $\phi=30$ deg, 45 deg, and 60 deg. The fits are close for the 2DTBCs with inclinations 30 deg and 45 deg. For 60 deg, the fits are not close, and for the largest specimen, the peak load was significantly overestimated (this discrepancy might, of course, be due to experimental error).

Figure 7 shows the distributions of the crack opening stress at peak load for all the specimens of 2DTBC with 30 deg inclined braiders. Figures 8 and 9 show the stress distributions at peak load for the same stress component, for the specimens of 2DTBC with 45 deg and 60 deg inclined braiders. Note that the peak stresses are, and should be, lower than the tensile strength f'_t on the microplanes; the reason is that the tensile peak stress depends not only on f'_t but also on the shear resistance, the damage evolution and localization, and the contribution of microplane stresses to the stress tensor reduced by volume fraction of tows.

The figures show that for smaller sizes, the fracture process zone occupies a larger percentage of the total volume and vice versa for larger sizes. Hence, for very large sizes compared with

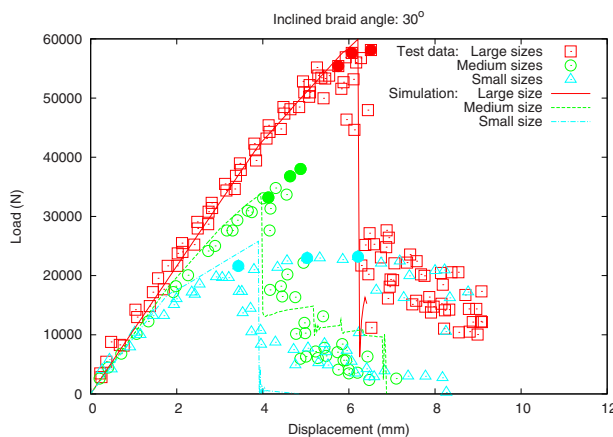


Fig. 4 Results from size effect tests of large-size, medium-size, and small-size 2DTBC specimens with an inclination angle $\phi=30$ deg of inclined braids and their simulation by microplane model for 2DTBC

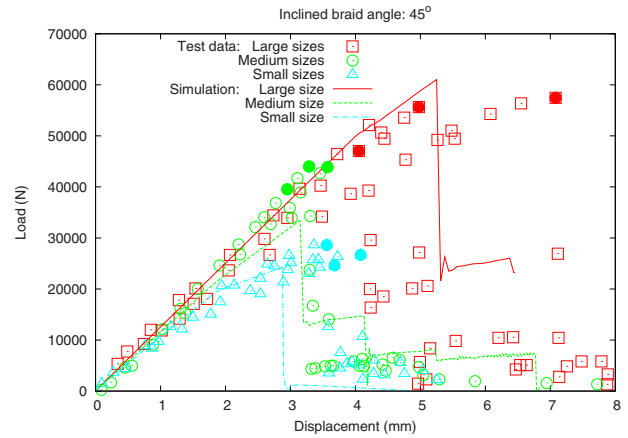


Fig. 5 Results from size effect tests of large-size, medium-size, and small-size 2DTBC specimens with an inclination angle $\phi=45$ deg of inclined braids and their simulation by microplane model for 2DTBC

l_{ch} , it is expected that the fracture process zone would become negligible, linear elastic fracture mechanics would apply, and the post-peak softening law would become irrelevant. Conversely, for small enough sizes, the softening distributed damage dominates and must be captured by the constitutive law.

Figure 10 shows the plot of force versus relative displacement in which the solid curve is a prediction by the model, and the symbols represent the experimental data obtained in a compact tension test. The model reasonably predicts the peak load, albeit with a small shift in the load-point relative displacement, and the post-peak response seems reasonable. Figure 11 shows the opening mode stress distribution on the compact tension test specimen immediately after the peak load.

4 Input Data and Calibration of Cohesive Fracturing Behavior

As the input, the following parameters must be specified: The volume fractions of the axial and inclined tows, the volume fraction of pure matrix between the tows, the angle between the braider and axial tows, the maximum out-of-plane slopes of the undulating tows, and the transversely isotropic elastic properties of all the fiber tows, which can be calculated from a mesome-

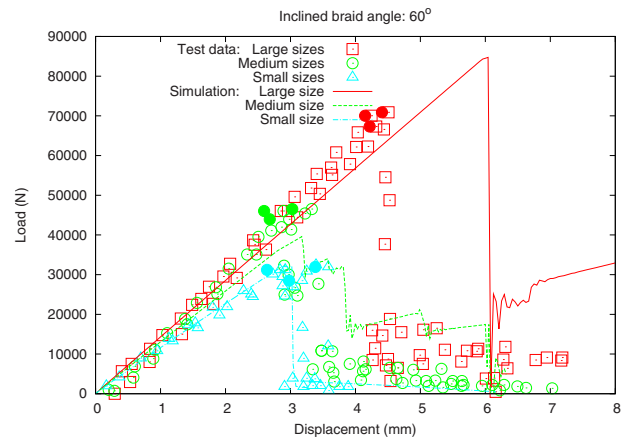


Fig. 6 Results from size effect tests of large-size, medium-size, and small-size 2DTBC specimens with an inclination angle $\phi=60$ deg of inclined braids, compared with computer results with the microplane model for 2DTBC

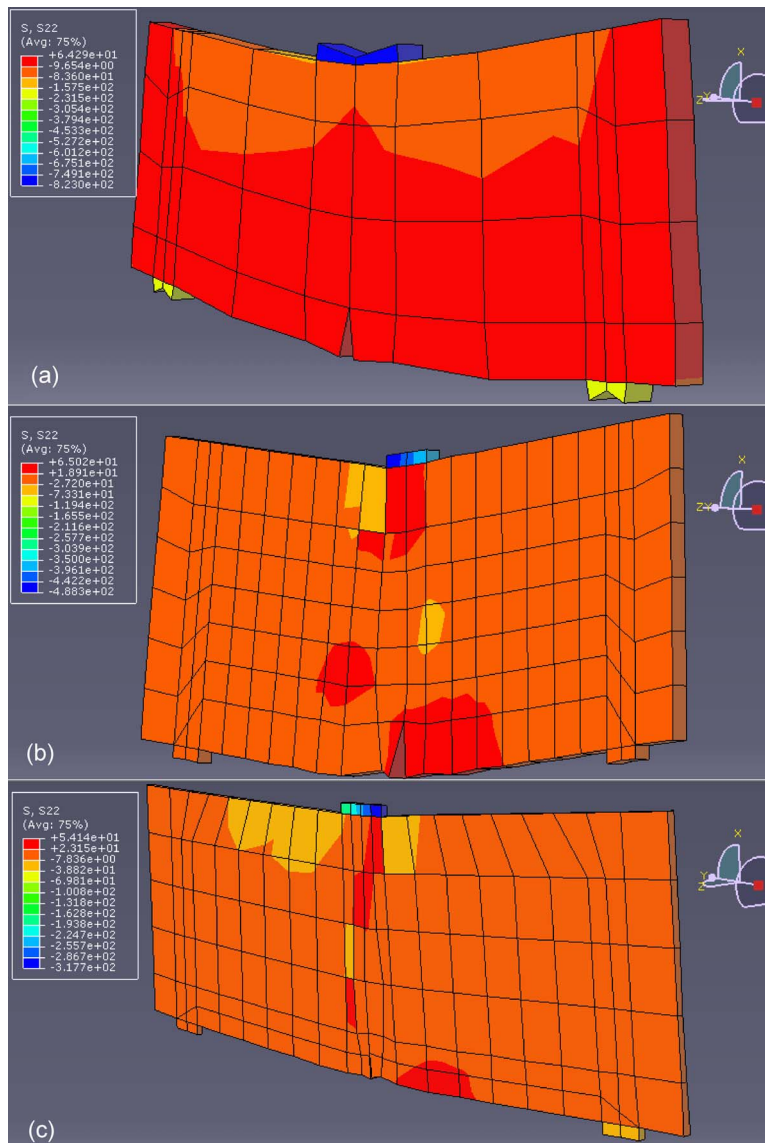


Fig. 7 Stress distribution in (a) small-size, (b) medium-size, and (c) large-size 2DTBC specimens with an inclination angle $\phi=30$ deg of inclined braids as predicted by microplane model for 2DTBC (the figures are scaled to the same width, and the finite element sizes were the same for all specimen sizes; S22 is the normal stress perpendicular to notch plane)

chanical model, e.g., Ref. [9] (used here) or Ref. [34] if sufficient explicit experimental data for this purpose are unavailable.

The cohesive fracturing behavior depends on the fracturing parameters of the matrix phase as well as the inclination angle of the bias tows. The present numerical results are obtained for a matrix with tensile strength $f_t=86$ MPa and with fracturing energy per unit volume $\gamma_f=0.915$ MPa. This energy represents the area under the complete stress-strain curve of the matrix, including the post-peak softening, and characterizes the average behavior over the width of the fracture process zone or of the crack band.

Based on the present data fitting, the cohesive law for braider angles of 30 deg, 45 deg, and 60 deg is characterized by the parameters listed in Table 3. For intermediate angles, the parameter values can be estimated by interpolating the data in this table.

Prediction of the composite properties from the constituents is difficult. It is complicated by the fact that the polymer matrix within the tows behaves very differently from the pure matrix in the bulk. Such differences have already been documented by other investigators, e.g., Ref. [3]. The average strength of the matrix in

the composite is reduced by the local stress concentrations around the microscale fibers and possible partial debonding of the fibers. More important could be the boundary layers of the matrix that must exist at the surfaces of the fibers. The volume of these layers may be of the same order of magnitude as the total matrix volume since the surface area of all the microscale fibers is very large. The thickness of these boundary layers is probably equal to the length of the macromolecular chains of the polymer, and the orientation of these chains may be predominantly parallel to the fiber surface, which may conceivably cause the boundary layers to be softer and less strong than the bulk polymer.

Thus, it is not surprising that close fitting of the fracture data for the 2DTBC requires the strength of the matrix in the composite to be equal to about 25% of the strength of the pure matrix in the bulk. In other words, the cohesive curve must be scaled down by the factor of 1/4. Note, however, that such estimates of matrix strength reduction are not universal. Other composite systems may exhibit different strength reduction factors. Nevertheless, the stated rationale may be extended to other systems.

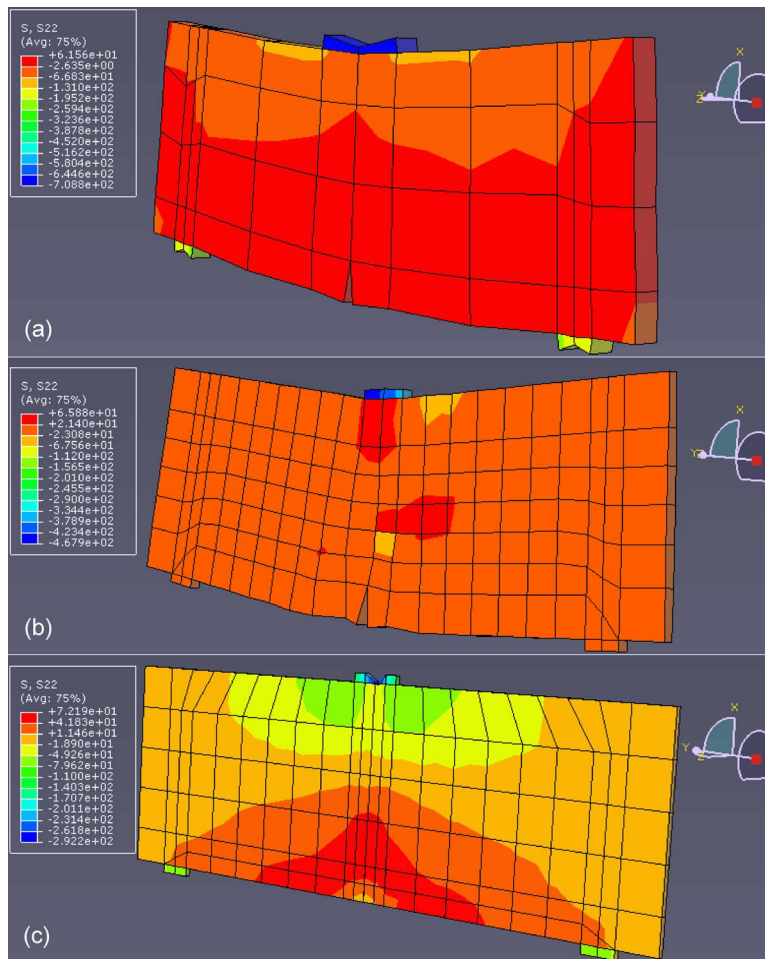


Fig. 8 Stress distribution in (a) small-size, (b) medium-size, and (c) large-size 2DTBC specimens with an inclination angle $\phi=45$ deg of inclined braids as simulated by microplane model for 2DTBC (the figures are scaled to the same width, and the finite element sizes were the same for all specimen sizes; S22 is the normal stress perpendicular to notch plane)

The fracture energy of the pure matrix is generally not reported by the material suppliers. However, a crude estimate can be based on the fact that the fracturing energy per unit volume is proportional not only to the tensile strength but also to the ductility, i.e., the limit strain at which the stress gets reduced to zero. Data fitting reveals that this limit strain must be scaled down by the factor of about 0.1. This can mean that to fit the data, the fracturing energy of the matrix in the composite must be about 40-times smaller than that of the pure matrix in the bulk.

5 Simulation of Axial Crushing of a Braided Tube by a Divergent Plug

The calibrated microplane model has been used to simulate, with no change in the material parameters, the experimental data obtained from a static axial crush test of a two-layer thick 30 deg 2DTBC tube of 100 mm length and 59.69 mm external radius. The tube is crushed by a diverging plug moving at velocity of 0.2 mm/s. Figure 12 presents a section of the geometry of the tube test. Figure 13 shows the simulation results and their comparison to the test data. Figure 14 depicts the mesh for one quarter of the tube and also shows the stress distribution in the direction of the tube axis.

The numerical simulations are presented for three different values of fracture energy. Initially, up to the peak load, the simulation results coincide. For the larger fracture energy, shown with the

thin curve, the response fluctuates with large amplitudes similar to the initial part of the experimental data. This curve also is a prediction by the model because the model parameters are the same as those determined in the size effect test simulations. Later, however, the fluctuation of the simulations becomes too large. Still, the energy dissipated, as calculated from the area under the curve, approximates reasonably well the experimental value.

The curve for the intermediate value of the fracture energy, shown with dashed lines, fits the test data best because the energy dissipated is approximated more closely. The peak load also is captured. This clearly indicates that depending on the interaction between the plug and the tube, the apparent fracture energy may change.

For the smallest fracture energy, the fluctuations after the peak load are milder but the energy dissipated gets overestimated. This second curve is plotted to show that the model can be calibrated by the test of crushing of a tube of one kind and then used in the simulations of tubes of other kinds.

The load carrying mechanism of the crushing 2DTBC tube consists of circumferential tensile straining enforced by the advance of the diverging plug. This produces very large, nearly uniform, tensile strains with cracks almost regularly spaced along the circumference of the tube. This experimentally observed mode of deformation is closely reproduced by the numerical simulations. The results show that for larger values of fracture energy, some strain localization can take place because otherwise sudden drops

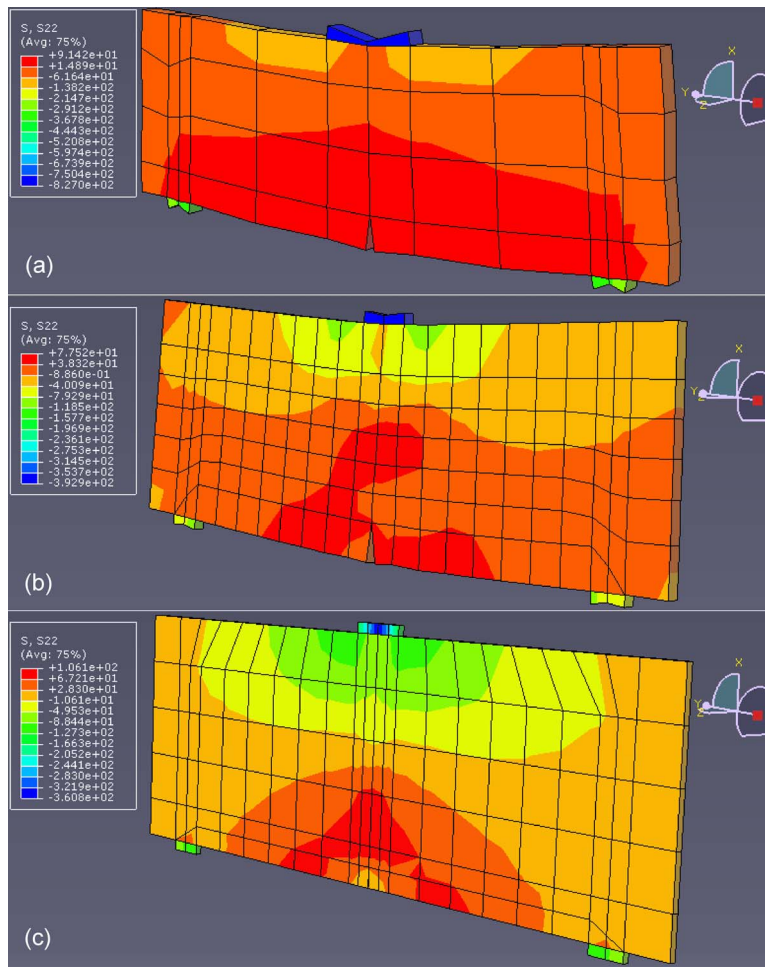


Fig. 9 Stress distribution in (a) small-size, (b) medium-size, and (c) large-size 2DTBC specimens with an inclination angle $\phi=60$ deg of inclined braids as simulated by microplane model for 2DTBC (the figures are scaled to the same width, and the finite element sizes were the same for all specimen sizes; S22 is the normal stress perpendicular to notch plane)

in the predicted reaction force cannot be explained. The results also show that for small enough values of fracture energy, almost no strain localization takes place and circumferential tensile strains are uniformly distributed.

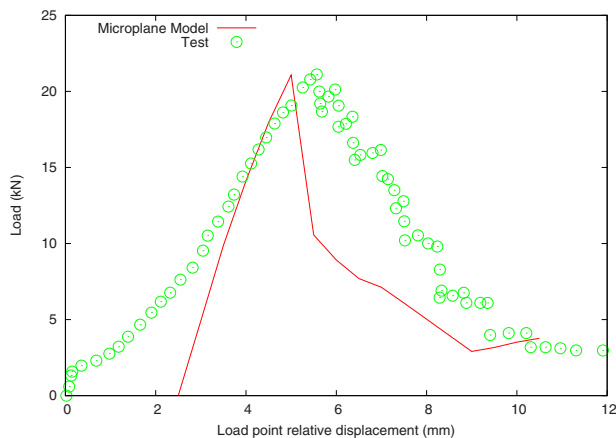


Fig. 10 Prediction by the model of the compact tension test (of a specimen made of 2DTBC with an inclination angle $\phi=30$ deg of inclined braids as shown in Fig. 11)

At the same time, the slabs delimited by adjacent axial cracks in the composite behave as beam-columns whose axial reaction significantly helps in resisting the plug advance. The axial reaction on the plug is mainly controlled by the buckling resistance of the beam-columns. Thus, it is not surprising that, in the simulations, the computer results improve when a larger number of elements through the thickness are used because the bending of the beam-column strips can be represented more faithfully. An additional contribution to the axial resisting force on the plug is the sliding friction between the plug and the tube but this has been neglected in the present simulations.

To match the test results, the finite elements, once highly deformed beyond a certain strain limit, have usually been removed from the system in previous finite element simulations. One reason has been that the Jacobian turned negative. But this negativity suggests that the constitutive law for large strains may have been incorrect. No such unrealistic, though expedient, artifice has been necessary in the present simulations.

6 Conclusions

The microplane model is an effective approach to the elastic and fracturing behavior of braided composites, suitable for implementation as a user subroutine in the ABAQUS/EXPLICIT commercial finite element program.

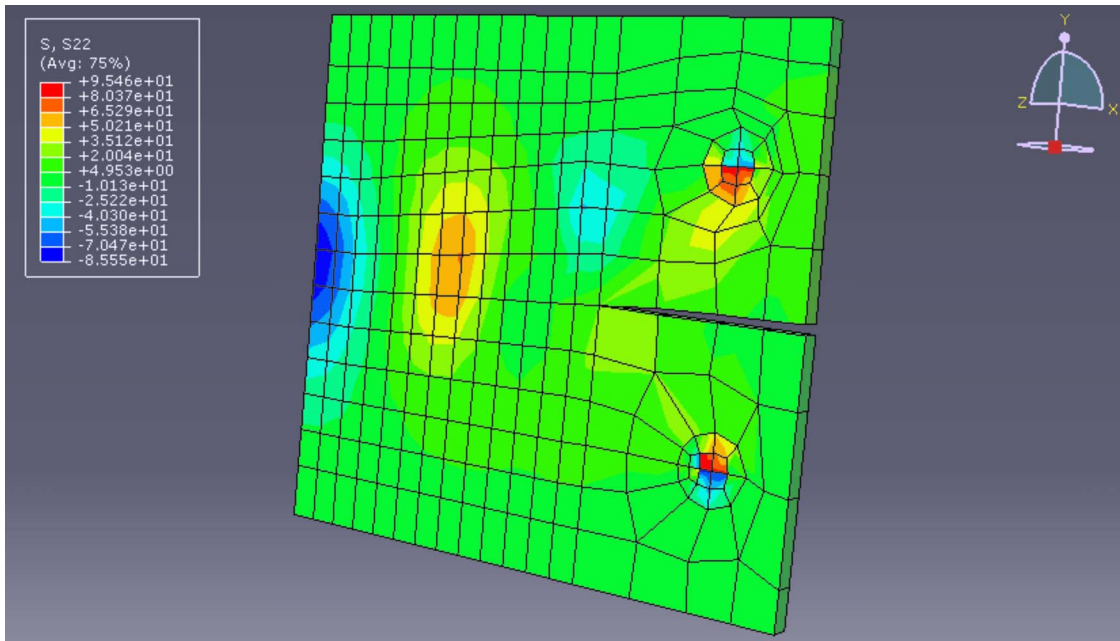


Fig. 11 The opening mode stress distribution in the compact tension test specimen immediately after the peak load

The size effect tests of notched beams standardized by RILEM are a good way to calibrate the model of fracturing behavior of braided composites.

For the 30 deg and 45 deg 2DTBCs, the fits are found to be good. For 60 deg 2DTBC, the fits are less accurate but still acceptable, and the peak load for the largest size specimens is over-estimated.

In the axial tube crush test with the plug speed considered, the simulated first 11 mm of the plug displacement are found to match the observed behavior quite closely. Later on, however, the calculated resisting force fluctuates excessively and decreases with a diminishing mass density toward realistic values.

The largest energy dissipation is obtained for the 30 deg 2DTBC, while the largest strength is obtained for the 60 deg 2DTBC. A compromise between the strength and dissipation is exhibited by the 45 deg 2DTBC.

Since maximizing the energy absorption during the tube crush is of prime interest, the 30 deg braider architecture in which the axial tows are parallel to the major axis of the tube seems to perform best.

Three simulations, one corresponding to the prediction by the model and others corresponding to smaller fracture energies, show that the model is capable of capturing the peak load and predicting the absorbed energy with reasonable accuracy.

For the larger values of fracture energy, some strain localization takes place, causing a sudden drop in the simulated reaction force. For small enough values of fracture energy, almost no strain localization takes place and circumferential tensile strains are uniformly distributed.

Acknowledgment

This research was supported by the Automotive Composites Consortium (ACC) under the U.S. Automotive Materials Partnership (USAMP) Cooperative Agreement No. DE-FC05-95OR22363 with the Department of Energy (US-DOE). The authors are grateful for the support and monitoring of the Predictive Technology Development and Crash Energy Management Group (ACC100). The authors acknowledge that this research was

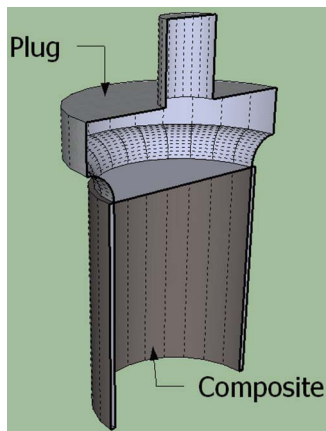


Fig. 12 The cross section of the setup for the crushing of tube specimens made of 2DTBC using a steel plug

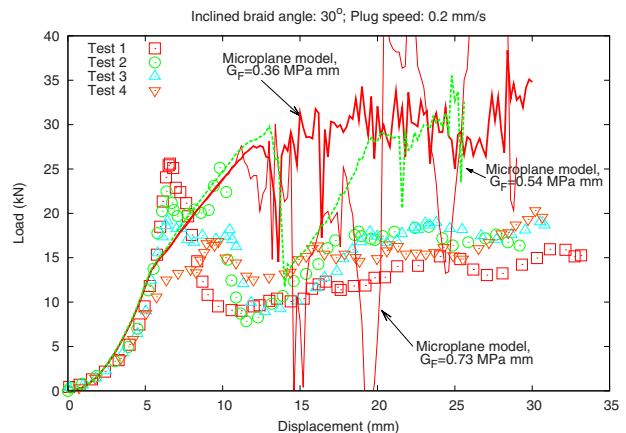


Fig. 13 Results from crush tests of tubes made of 2DTBC specimens with an inclination angle $\phi=30$ deg of inclined braids and their simulation by microplane model for 2DTBC

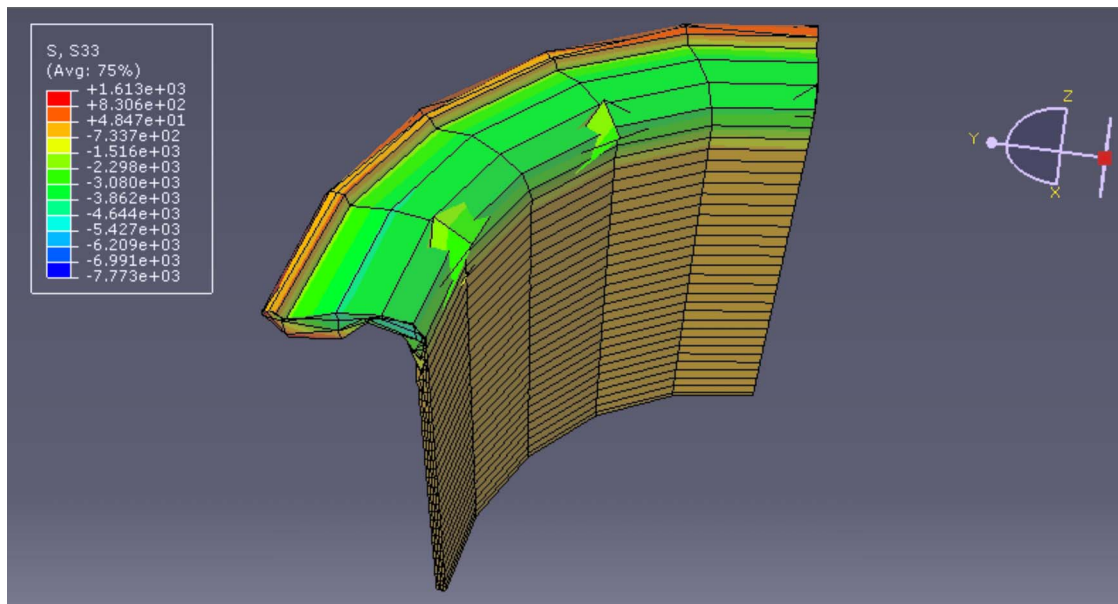


Fig. 14 Stress distribution in the tube after the plug displacement of 14 mm as obtained by microplane model for 2DTBC

funded, in whole or in part, by the US-DOE, and that such support does not constitute an endorsement by the US-DOE of the views expressed herein. Additional support for the underlying theoretical aspects was received from the Initiative for Sustainability and Energy (ISEN) at Northwestern University.

References

- [1] Cox, B. N., Dadkhah, M. S., Morris, W. L., and Flintoff, J. G., 1994, "Failure Mechanisms of 3D Woven Composites in Tension, Compression, and Bending," *Acta Metall. Mater.*, **42**, pp. 3967–3984.
- [2] Quek, S. C., Waas, A. M., Shahwan, K. W., and Agaram, V., 2004, "Compressive Response and Failure of Braided Textile Composites: Part I Experiments," *Int. J. Non-Linear Mech.*, **39**(4), pp. 635–648.
- [3] Song, S., Waas, A. M., Shahwan, K. W., Xiao, X., and Faruque, O., 2007, "Braided Textile Composites Under Compressive Loads: Modeling the Response, Strength and Degradation," *Compos. Sci. Technol.*, **67**(15–16), pp. 3059–3070.
- [4] Chou, T.-W., 1992, *Microstructural Design of Fiber Composites*, Cambridge Solid State Science Series, Cambridge University Press, Cambridge, UK.
- [5] Dadkhah, M. S., Cox, B. N., and Morris, W. L., 1995, "Compression—Compression Fatigue of 3D Woven Composites," *Acta Metall. Mater.*, **43**(12), pp. 4235–4245.
- [6] Bažant, Z. P., and Cedolin, L., 1991, *Stability of Structures*, Oxford University Press, Oxford, NY and (3rd Ed., World Scientific Publishing, Singapore and London, 2010).
- [7] Bažant, Z. P., 1968, "Effect of Folding of Reinforcing Fibers on the Elastic Moduli and Strength of Composite Materials," *Mekh. Polim.*, **4**, pp. 314–321 (in Russian).
- [8] Waas, A. M., and Schultheisz, C. R., 1996, "Compressive Failure of Composites, Part II: Experimental Studies," *Prog. Aerosp. Sci.*, **32**(1), pp. 43–78.
- [9] Quek, S. C., Waas, A. M., Shahwan, K. W., and Agaram, V., 2003, "Analysis of 2D Triaxial Flat Braided Textile Composites," *Int. J. Mech. Sci.*, **45**, pp. 1077–1096.
- [10] Quek, S. C., Waas, A. M., Shahwan, K. W., and Agaram, V., 2003, "Compressive Response and Failure of Braided Textile Composites: Part 2—Computations," *Int. J. Non-Linear Mech.*, **39**(4), pp. 650–663.
- [11] Whitcomb, J. M., and Noh, J., 2000, "Concise Derivation of Formulas for 3D Sublaminar Homogenization," *J. Compos. Mater.*, **34**, pp. 522–535.
- [12] Sankar, B. V., and Marrey, R. V., 1993, "A Unit-Cell Model of Textile Composite Beams for Predicting Stiffness Properties," *Compos. Sci. Technol.*, **49**, pp. 61–69.
- [13] Bažant, Z. P., Adley, M. D., Carol, I., Jirásek, M., Akers, S. A., Rohani, B., Cargile, J. D., and Caner, F. C., 2000, "Large-Strain Generalization of Microplane Model for Concrete and Application," *J. Eng. Mech.*, **126**(9), pp. 971–980.
- [14] Bažant, Z. P., Caner, F. C., Carol, I., Adley, M. D., and Akers, S. A., 2000, "Microplane Model M4 for Concrete: I. Formulation With Work-Conjugate Deviatoric Stress," *J. Eng. Mech.*, **126**(9), pp. 954–961.
- [15] Bažant, Z. P., Caner, F. C., Adley, M. A., and Akers, S. A., 2000, "Incorporation of Rate Effects of Fracturing and Creep Into Microplane Model for Concrete Dynamics," *J. Eng. Mech.*, **126**(9), pp. 962–970.
- [16] Bažant, Z. P., and Ozbolt, J., 1990, "Nonlocal Microplane Model for Fracture, Damage, and Size Effect in Structures," *J. Eng. Mech.*, **116**(11), pp. 2484–2504.
- [17] Bažant, Z. P., and Prat, P. C., 1988, "Microplane Model for Brittle Plastic Material: I. Theory," *J. Eng. Mech.*, **114**, pp. 1672–1688.
- [18] Bažant, Z. P., and Prat, P. C., 1988, "Microplane Model for Brittle Plastic Material: II. Verification," *J. Eng. Mech.*, **114**, pp. 1689–1702.
- [19] Bažant, Z. P., and Oh, B.-H., 1983, "Microplane Model for Fracture Analysis of Concrete Structures," Proceedings of the First International Symposium on the Interaction of Non-Nuclear Munitions With Structures, U.S. Air Force Academy, Colorado Springs, CO, pp. 49–53.
- [20] Bažant, Z. P., and Oh, B.-H., 1985, "Microplane Model for Progressive Fracture of Concrete and Rock," *J. Eng. Mech.*, **111**, pp. 559–582.
- [21] Bažant, Z. P., and Oh, B.-H., 1986, "Efficient Numerical Integration on the Surface of a Sphere," *ZAMM*, **66**(1), pp. 37–49.
- [22] Carol, I., and Bažant, Z. P., 1997, "Damage and Plasticity in Microplane Theory," *Int. J. Solids Struct.*, **34**(29), pp. 3807–3835.
- [23] Carol, I., Bažant, Z. P., and Prat, P. C., 1991, "Geometric Damage Tensor Based on Microplane Model," *J. Eng. Mech.*, **117**(10), pp. 2429–2448.
- [24] Brocca, M., and Bažant, Z. P., 2000, "Microplane Constitutive Model and Metal Plasticity," *Appl. Mech. Rev.*, **53**(10), pp. 265–281.
- [25] Cusatis, G., Beghini, A., and Bažant, Z. P., 2008, "Spectral Stiffness Microplane Model for Quasi-Brittle Composite Laminates—Part I: Theory," *ASME J. Appl. Mech.*, **75**(2), p. 021009.
- [26] Bažant, Z. P., 2010, "Can Multiscale-Multiphysics Methods Predict Softening Damage and Structural Failure?," *Int. J. Multiscale Comp. Eng.*, **8**(1), pp. 61–67.
- [27] Bažant, Z. P., and Grassl, P., 2007, "Size Effect of Cohesive Delamination Fracture Triggered by Sandwich Skin Wrinkling," *ASME J. Appl. Mech.*, **74**, pp. 1134–1141.
- [28] Ishikawa, T., and Chou, T. W., 1982, "Elastic Behavior of Woven Hybrid Composites," *J. Compos. Mater.*, **16**(1), pp. 2–19.
- [29] Miravete, A., 1999, *3-D Textile Reinforcements in Composite Materials*, Woodhead Publishing Ltd., Cambridge, UK.
- [30] Naik, N. K., and Stembekar, P. S., 1992, "Elastic Behaviour of Woven Fabric Composites: I—Lamina Analysis," *J. Compos. Mater.*, **26**, pp. 2196–2225.
- [31] Huang, Z. M., 2000, "The Mechanical Properties of Composites Reinforced With Woven and Braided Fabrics," *Compos. Sci. Technol.*, **60**, pp. 479–498.
- [32] Naik, R., 1996, "Analysis of 2D Triaxial and 3D Multi-Interlock Braided Textile Composites," 37th AIAA/ASME/ASCE/AHS/ASC Structures, Structural Dynamics and Materials Conference.
- [33] Cox, B. N., and Dadkhah, M. S., 1995, "The Macroscopic Elasticity of 3D Woven Composites," *J. Compos. Mater.*, **29**, pp. 785–819.
- [34] Šmilauer, V., Hoover, C. G., Bažant, Z. P., Caner, F. C., Waas, A. M., and Shahwan, K. W., 2009, "Numerical Simulation of Fracture of Braided Composites via Embedded Representative Unit Cell," Northwestern University, Theoretical and Applied Mechanics Report; Engineering Fracture Mechanics 2010, in press.
- [35] Song, S., Waas, A. M., Shahwan, K. W., Faruque, O., and Xiao, X., 2008, "Compression Response of 2D Braided Textile Composites: Single Cell and Multiple Cell Micromechanics Based Strength Predictions," *J. Compos.*

- Mater., **42**(23), pp. 2461–2482.
- [36] Bažant, Z. P., 2002, *Scaling of Structural Strength*, Hermes Penton Science, London.
- [37] Bažant, Z. P., and Planas, J., 1998, *Fracture and Size Effect in Concrete and Other Quasibrittle Materials*, CRC, Boca Raton, FL.
- [38] Bažant, Z. P., 1984, “Size Effect in Blunt Fracture: Concrete, Rock, Metal,” *J. Eng. Mech.*, **110**(4), pp. 518–535.
- [39] Bažant, Z. P., 2004, “Probability Distribution of Energetic-Statistical Size Effect in Quasibrittle Fracture,” *Probab. Eng. Mech.*, **19**(4), pp. 307–319.
- [40] Dassault Systèmes, 2007, Dassault Systèmes of America Corp., 6320 Canoga Avenue, Trillium East Tower, Woodlands Hills, CA 91367-2526.
- [41] Adley, M. D., Frank, A. O., and Danielson, K. T., “The High-Rate Brittle Microplane Concrete Model: Part I: Bounding Curves and Quasi-Static Fit to Material Property Data,” *Comput. Concr.*, submitted.
- [42] Frank, A. O., Adley, M. D., Danielson, K. T., and McDevitt, H. S., Jr., “The High-Rate Brittle Microplane Concrete Model: Part II: Application to Projectile Perforation of Concrete Slabs,” *Comput. Concr.*, submitted.
- [43] Bažant, Z. P., 2004, *Scaling of Structural Strength*, 2nd ed., Elsevier, London.
- [44] Bažant, Z. P., Daniel, I. M., and Li, Z., 1996, “Size Effect and Fracture Characteristics of Composite Laminates,” *ASME J. Eng. Mater. Technol.*, **118**(3), pp. 317–324.
- [45] Bažant, Z. P., Kim, J.-J. H., Daniel, I. M., Becq-Giraudon, E., and Zi, G., 1999, “Size Effect on Compression Strength of Fiber Composites Failing by Kink Band Propagation,” *Int. J. Fract.*, **95**, pp. 103–141.
- [46] Bažant, Z. P., Zhou, Y., Novák, D., and Daniel, I. M., 2004, “Size Effect on Flexural Strength of Fiber-Composite Laminate,” *ASME J. Eng. Mater. Technol.*, **126**(1), pp. 29–37.
- [47] Bažant, Z. P., Zhou, Y., Daniel, I. M., Caner, F. C., and Yu, Q., 2006, “Size Effect on Strength of Laminate-Foam Sandwich Plates,” *ASME J. Eng. Mater. Technol.*, **128**(3), pp. 366–374.
- [48] Bayldon, J. M., Bažant, Z. P., Daniel, I. M., and Yu, Q., 2006, “Size Effect on Compressive Strength of Sandwich Panels With Fracture of Woven Laminate Facesheet,” *ASME J. Eng. Mater. Technol.*, **128**, pp. 169–174.
- [49] Waas, A. M., 2009, private communication.
- [50] Bažant, Z. P., 1990, “Size Effect Method for Determining Fracture Energy and Process Zone Size of Concrete,” *Mater. Struct.*, **23**, pp. 461–465.
- [51] Cervenka, J., Bažant, Z. P., and Wierer, M., 2005, “Equivalent Localization Element for Crack Band Approach to Mesh-Sensitivity in Microplane Model,” *Int. J. Numer. Methods Eng.*, **62**(5), pp. 700–726.
- [52] Yu, Q., Le, J.-L., Hoover, C. G., and Bažant, Z. P., 2010, “Problems With Hu-Duan Boundary Effect Model and Its Comparison to Size-Shape Effect Law for Quasibrittle Fracture,” *J. Eng. Mech.*, **136**(1), pp. 40–50.